Surface & Coatings Technology 295 (2016) 112–118

Contents lists available at ScienceDirect

Surface & Coatings Technology

journal homepage: www.elsevier.com/locate/surfcoat

Tetrakis(trimethylsilyloxy)silane for nanostructured SiO_2-like films deposited by PECVD at atmospheric pressure

J. Schäfer [a,*], J. Hnilica [b], J. Šperka [b,c], A. Quade [a], V. Kudrle [b], R. Foest [a], J. Vodák [d], L. Zajíčková [b,c]

[a] Leibniz Institute for Plasma Science and Technology e.V., Felix-Hausdorff-Straße 2, 17489 Greifswald, Germany
[b] Department of Physical Electronics, Masaryk University, Kotlářská 2, CZ-61137 Brno, Czech Republic
[c] CEITEC — Central European Institute of Technology, Masaryk University, Kamenice 753/5, CZ-62500 Brno, Czech Republic
[d] Institute of Physical Engineering, Faculty of Mechanical Engineering, Brno University of Technology, Technická 2896/2, CZ-61669 Brno, Czech Republic

ARTICLE INFO

Article history:
Received 16 May 2015
Revised 21 August 2015
Accepted in revised form 26 September 2015
Available online 3 October 2015

Keywords:
Tetrakis(trimethylsilyloxy)silane
Tetrakis(trimethylsiloxy)silane
Plasma jet
Silicon dioxide

ABSTRACT

Plasma enhanced chemical vapor deposition (PECVD) from tetrakis(trimethylsilyloxy)silane (TTMS) has been studied at atmospheric pressure. TTMS has been chosen because of its unique 3D structure with potential to form nano-structured organosilicon polymers. Despite the widespread surveying of various silicon-organic molecules for PECVD, the use of TTMS in AP-PECVD has not been investigated deeper yet. PECVDs have been performed with two different plasma jets. While they are alike regarding the geometry and injection of TTMS, they differ in input power and excitation frequency. The radiofrequency plasma jet operates at lower power densities as compared to the microwave plasma jet. Despite this all the deposited films exhibit similar chemical properties resembling that of silicon dioxide (Si:O = 1:2) with carbon content below 5%. The films demonstrate a broad variety of morphologies from compact smooth films to nano-dendritic 3D structures depending on the particular process.

© 2015 Elsevier B.V. All rights reserved.

1. Introduction

If complex organosilicon precursors are used for PECVD, the chemistry and properties of the resulting films are heavily influenced by the operational conditions. Depending on temperature, power density or gas mixture (e.g. oxygen content) inorganic SiO_2 [1,2] films are observed as well as branched and/or cross-linked structures of polymethylsiloxanes [3]. Often, the incorporation of a high content of organic functional groups, in particular methyl groups is causing a porous or less dense film structure with inferior chemical and mechanical stability. Hence, the independent adjustment of the morphological and chemical film properties by variation of the process parameters at atmospheric pressure is a challenging task. Much of current effort is dedicated to this issue [4,5]. In particular, a stability against chemical or mechanical impact is desirable for coatings in a wide range of morphologies. For instance, permeation barriers rely on compact pin-hole free coatings [6] whereas surfaces for heterogeneous catalysis require hierarchically nano-structured films with large surface area and their catalysts centered in chemically stable matrices [7,8]. The importance of hybrid materials production from molecular precursors leads to investigation of organosilicates from complex precursors. For example, precursors of the general formula $(CH_3O)_3SiRSi(OCH_3)_3$ are under investigation for the preparation of hybrid materials by sol-gel polycondensation [9].

In the present study it is demonstrated that such different morphological structures can be obtained using tetrakis(trimethylsilyloxy)silane (TTMS, $C_{12}H_{36}O_4Si_5$) as thin film precursor for PECVD, while the chemical composition remains essentially SiO_2–like. Among other complex silicon organic molecules commonly in use for PECVD, the TTMS molecule (see Fig. 1) exhibits several advantages, with regard to forming structured coatings at suitable conditions. The molecular structure of TTMS is characterized by the presence of five rigid tetrahedral sub-units: the central unit SiO_4 and four peripheral units $OSi(CH_3)_3$. The central unit represents the elementary cell of quartz-like structures in dense SiO_2 films. The average valence angle of SiOSi in TTMS is 146° [10] and hence wider than in usually used hexamethyldisiloxane (HMDSO, $(CH_3)_3Si–O–Si(CH_3)_3$) where 130° is found [11]. Thus, the rotation around the Si^c–O bonds[1] in TTMS is virtually more unrestricted than in HMDSO. This causes a relatively flexible conformation of TTMS [12]. Consequently, this flexible conformation can play a crucial role for the self-adapted growth of nanostructured films. In addition, this precursor is non-flammable, nontoxic, and has reasonably high vapor pressure. After studies [13] and [14], the present work is the first utilizing TTMS in atmospheric pressure high-frequency PECVD processes.

* Corresponding author.
E-mail address: jschaefer@inp-greifswald.de (J. Schäfer).

[1] The index ^{c} denotes the central atom of the molecules.

http://dx.doi.org/10.1016/j.surfcoat.2015.09.047
0257-8972/© 2015 Elsevier B.V. All rights reserved.

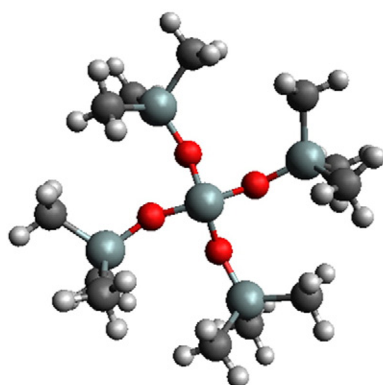

Fig. 1. Molecule of tetrakis(trimethylsilyloxy)silane (TTMS $C_{12}H_{36}O_4Si_5$).

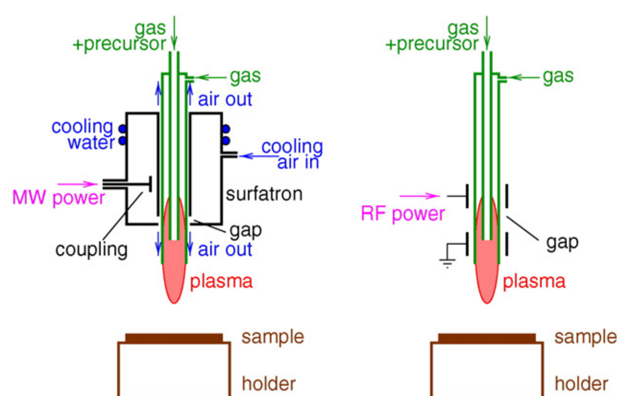

Fig. 2. Comparison of two plasma jet set-ups.

Plasma enhanced chemical vapor deposition of silicon-organic films at atmospheric pressure (AP-PECVD) is commonly performed with a wide variety of precursors [15–18]. The most prominent class of precursors in use is alcoxysilanes (e.g. hexamethyldisyloxane, HMDSO, tetramethyldisiloxane, TMDSO, tetraethoxysilane, TEOS, triethoxysilane, TriEOS) or hexamethyldisilazane, HMDSN. Their widespread usage is lessening their purchase price which further alleviates their application for technological processes. Furthermore they are in use because of their uncomplicated handling, non-toxicity and simple vaporization at room temperature. Often the studies of the film deposition processes are directed to obtain chemically and morphologically homogeneous coatings [19]. From this point of view, the investigation of structural variations in AP-PECVD using complex organosilicon precursors represents a rare objective with an interesting technological potential [4,20].

2. Experimental set-up

In this paper, we present a comparative study of AP-PECVD using two different plasma jets: a MW plasma jet and a radiofrequency (RF) plasma jet described in previous experiments [19,21]. The MW jet does not allow the operation at low power ranges (below 100 W), whereas the main operating range of the RF jet is typically below 20 W. Here, we disregard the differences in the plasma kinetics of both devices caused by their different excitation schemes. Despite being operated at different excitation frequencies their experimental arrangement is quite similar, see Fig. 2. We keep the geometry of the jets and precursor injection similar in both experiments and consider the differing power densities as the most significant disparity in the first approximation. Using both jets then effectively covers a wider power range. The usage of an extensive surface and material analytics allows discussing the relationship of homogeneity, type of nanostructuring and chemical composition of the deposited films.

2.1. Microwave jet

The atmospheric pressure microwave electrode-less jet uses a surfatron [22] as excitation source (SAIREM Surfatron 80 type with integrated matching). This source is powered by a magnetron generator (SAIREM GMP 20 KED, 2.45 GHz, 0–2 kW) via ferrite circulator, waveguide and coaxial cable. The cable and coaxial connectors limit the supplied power to 300 W. During this study the microwave power was 235 W.

The surfatron excitation source consists of a tuned coaxial resonant cavity through which a fused silica discharge tube (80 mm long, 6 mm and 8 mm inner and outer diameter, respectively) is inserted. There is another silica coaxial capillary with 1 mm diameter in the center of this discharge tube. The supplied gas – argon – passes through the annulus between the capillary and the discharge tube. Its flow is maintained at 2.6 slm by a mass flowmeter.

Liquid TTMS is placed in a bubbler cylinder filled with glass beads. After passing the bubbler cylinder the auxiliary argon carrier gas flow (90 and 435 sccm) is enriched with TTMS vapors at laboratory temperature. Using the coaxial capillary this mixture is injected downstream the surfatron excitation gap into the active microwave discharge. The diffusion losses in the thin capillary prevent ignition of a discharge inside the capillary. TTMS vapor is dissociated in the discharge and forms a deposit on a sample placed 6 mm from discharge tube end. The amount of TTMS vapors introduced (0.02–0.07 g/h i.e. 0.02–0.07 sccm) is controlled by the auxiliary argon flow and verified using gravimetry. The adjusted rates of argon and TTMS provide the precursor concentration of 7 ppm to 23 ppm in order to study deposition conditions under variation of the plasma-chemically relevant parameter energy per molecule. Note that the only way to vary the specific energy in this particular microwave experiment is to adjust the gas management (flows).[2] Nevertheless, for both set-ups (MW and RF), the resulting relative concentrations of TTMS in the total argon flux have the same order of 10^{-5}. The duration of a deposition experiment is 5 min.

2.2. Radiofrequency jet

The atmospheric pressure radiofrequency plasma source consists of a fused silica tube (i.d. 4 mm, o.d. 6 mm) with two external ring electrodes. The electrodes are 5 mm wide and their distance is 5 mm. A coaxial thin-wall capillary with diameter of 1.9 mm is located in the center of the discharge tube. Similar to the MW jet, the dimension of the inner capillary does not impede the generation of a discharge inside the tube and no discharge is ignited inside the inner capillary due to diffusion losses. The substrate for film deposition is located 6 mm below the nozzle of the discharge tube.

Argon flow rates through the central capillary (inner Ar flow rate) and the annulus between the capillary and the discharge tube (outer Ar flow rate) are fixed at 1.0 slm and 0.5 slm, respectively. The coaxial flows are dimensioned such that the gas velocities in each of the capillaries fit to a simple parabolic velocity profile in the tube as without coaxial flux separation. Thus lateral fluxes are avoided. The setting of the optimal flow rates required to adapt the dosage of TTMS by means of a blower for a better comparability with the MW set-up. Instead of using a conventional bubbler arrangement, TTMS vapors are admixed to the inner Ar flow by flowing Ar above the liquid TTMS in the blower flask before the mixture enters the capillary at laboratory temperature of 23 °C. Indeed, the Ar flow of 1 slm through the blower carries the same flow rate of TTMS vapors, 0.02 sccm, as 0.09 sccm of argon through the bubbler in the MW jet set-up. This was checked by measuring the TTMS flow rates beforehand for various Ar flow rates in both the set-

[2] The variation of applied power would be feasible in principle; the energy support depends crucially on the resonance conditions which would be infringed by changing the applied power.

ups by gravimetry, i.e. weight loss of liquid TTMS after longer operation at constant conditions. The accuracy of the TTMS flow rates given in Table 1 is estimated as 10%.

The RF power (27.12 MHz, DTG2710, Dressler) supplied to the plasma was 6 or 15 W. This, along with the given flow ensures a source operation in a distinctive discharge mode with four azimuthally rotating discharge filaments dubbed Locked Mode 4 (LM4) and described in detail in [23]. Here, the time needed to deposit a film is longer: 15 min for one experiment.

3. Materials and methods

All experiments have been performed with a similar gas mixture, Argon (9.5, Linde or Messer Griesheim, resp.) to which a small amount of TTMS (Sigma-Aldrich, purity 97%) vapor was added. Because the usage of TTMS is uncommon for PECVD, we summarized the basic properties in Table 2. Thin films have been deposited on double side polished (DSP) silicon wafers, that are transparent in the middle infra red (IR) spectral range.

The resulting films have been analyzed with several methods in order to characterize their structuring and chemical composition. A morphological characterization has been carried out using atomic force microscopy (AFM, Dimension Icon microscope, Bruker) and high resolution scanning electron microscopy (HR-SEM). The SEM (JSM 7500F, JEOL) employs a field-emission gun. The secondary electron in-lens detector enables to observe structural features of the deposited films at a maximum specified resolution of 1.0 nm at 15 keV. The device can operate without any preparative coatings which could lead to morphological artifacts at nanometer scale. For the analysis of the vertical film structure, a cross-section ion polisher (CIP, JEOL) has been used. The chemical composition has been characterized by means of X-ray spectroscopy (EDX, Bruker X-Flash spectrometer, 30 mm^2 silicon drift droplet detector).

The elemental surface composition was analyzed with X-ray photoelectron spectroscopy (XPS) using an AXIS Ultra DLD electron spectrometer (Kratos Analytical). The spectra were recorded by means of monochromatic Al–K_α excitation (1486.6 eV) with a medium magnification (field of view 2) lens mode and by selecting the slot mode, providing an analysis area of approximately 25 μm in diameter. Charge neutralization was implemented by low energy electrons injected into the magnetic field of the lens from a filament located directly atop the sample. Data acquisition and processing were carried out using CasaXPS software, version 2.14dev29 (Casa Software Ltd.). To remove the uppermost layer of contaminating hydrocarbons the samples were sputtered for 5 min with 4.5 keV Ar-ions.

The thickness distribution of smooth coatings has been measured by means of spectral imaging reflectometry (ISR) [24]. The ISR spectra were measured at normal incidence of light in the spectral range between 270 and 900 nm with pixel size (spatial resolution) of 37 × 37 μm^2. They were fitted using the PJDOS dispersion model for SiO_2-like materials [25] in custom software as described in a previous work [24].

Fourier transform infra-red spectroscopy (FTIR) was configured for ATR (Attenuated Total Reflection, Spectrum One microscope, Perkin Elmer) and for transmission measurements (Bruker Vertex 80v).

Table 1
Deposition conditions for the films prepared by RF (27.12 MHz) and MW (2.45 · 10^3 MHz) plasma jets.

Sample	Power [W]	Ar outer [slm]	Ar inner [slm]	TTMS [sccm]	W/F [kJ cm^{-3}]
RF1	6	0.5	1.0	0.02	**20**
RF2	15	0.5	1.0	0.02	**50**
MW1	235	2.60	0.4	0.07	**200**
MW2	235	2.60	0.09	0.02	**900**

Table 2
Fundamental properties of TTMS (CAS Nr. 3555-47-3) [www.sigmaaldrich.com, www.arb.ca.gov].

Quantity	Unit	Value
Molecular mass	AMU	384.85
Boiling temperature at 267 Pa	°C	103.0–106.0
Flash point	°C	76
Density of liquid	g/cm^3	0.87
Vapor pressure at 25 °C	Pa	8.96

4. Results

From 20 produced and analyzed samples, four representative samples were chosen in order to demonstrate the general semi-quantitative changes of significant material properties and reveal the apparent relation to the specific energy per molecule of TTMS and on the used plasma source. We consider them representative of the trends and suitable for the discussion. The overview of experimental parameters for these four samples is given in Table 1. The Yasuda parameter i.e. specific energy per unit volume of TTMS precursor is calculated for each condition and plotted in the right column.

4.1. Morphology and structure

For the investigation of the structural features in the films a combined application of scanning electron microscopy and atomic force microscopy has been chosen. By this complementary approach apparent disproportional differences in the film morphology can be described depending on the precursor amount and specific energy for the PECVD. While SEM is suited preferably for the investigation of deeply and sharply structured forms, AFM is appropriate for the topographic description of more or less smooth samples. Here, the films deposited using the RF jet form uniform layers and they exhibit a comparably low surface roughness which has been characterized by AFM. On the other hand, the films produced by the MW jet demonstrated a fine-textured topography which has been investigated with SEM.

The texture of two SEM images (MW1 and MW2) is shown in Fig. 3. In the MW jet, the deposition mechanism leads to the growth and branching of nanoscopic auxiliary buds. Thus, three dimensional nanodendrites are formed. The spreading structure takes up a specific volume with a large free surface similar to a fractal. The fractalized parts of the top texture indicate narrow trenches reaching fully down to the initial points of the branched dendrites. Therefore, two detectors were utilized during the SEM characterization of the MW samples. The detector of the secondary emitted electrons (SEI) collects signals of top areas (focus on the lateral structure), while the detector of back scattered electrons (BEI) extracts information from deeper parts of the surface (focus on the vertical structure). Fig. 3 combines both images (SEI and BEI) by color-coding thus visualizing the degree of spatial spreading. In the case of lower energy per TTMS molecule (sample MW1), bigger rugged structures take a specific lateral dimension exceeding 5 μm. If the energy increases (sample MW2), more dense dendrites with lateral diameters between 1 to 3 μm can be observed. The effect can be explained with a faster deposition kinetics at higher specific energy. Indeed, a shorter reaction time limits the surface diffusion length. Therefore dimensions of the rugged topography are rescaled down for higher specific energy.

The cross-sections of the deposited films have been investigated deeper in order to explore the progression of the growth from the substrate to the top of the dendrites. The comparison between films deposited by the MW jet (sample MW2) and by the RF jet (sample RF2) is shown in Fig. 4. The ion beam polishing of the film cross-sections reveals the presence of an amazing vertical structure of the MW samples. The branched structure grows over several micrometers in vertical direction fully intact, see Fig. 4 and exhibits a fractal behavior. Moreover, at the bottom of the film an initial layer with a thickness of approximately

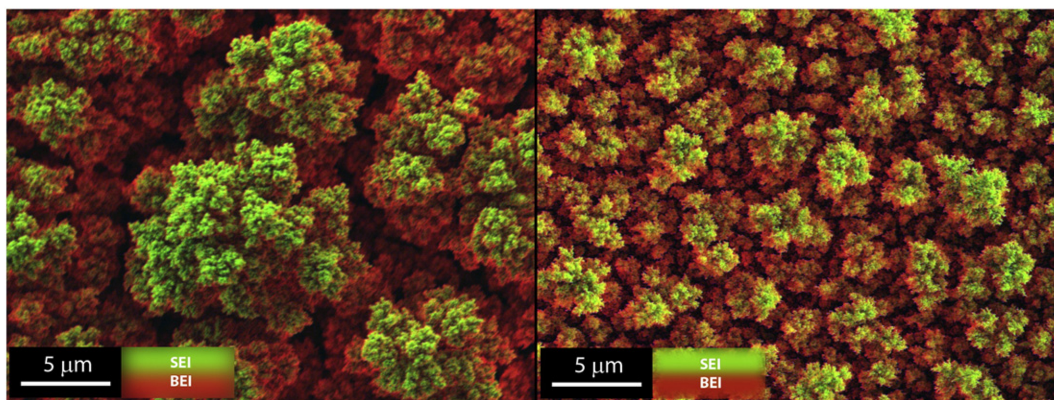

Fig. 3. SEM images taken by combined detection of back-scattered (SEI — green color) and secondary electrons (BEI — red color) from surfaces of MW1 (left image, lower specific energy) and MW2 (right image, higher specific energy) films.

200 nm has been observed. Because of the constant external conditions during the deposition, we assume that the transition from the initial layer to the dendrites results from a self-organized competition between parallel nucleation processes [26]. The continuous growth at points with a high nucleation dominates over points with a smaller nucleation. Such disturbance can occur at locally increased surface temperature, in particular at a higher specific energy in the MW experiment. The disturbance consequently stimulates an increasing roughness of the initial layer and leads to a growth of dendrites if sufficient energy is supplied. This is not the case for the deposition with the RF jet, where significantly less energy per TTMS molecule is coupled and evidently no structured morphology can be observed. Finally, the thickness of the deposited films (RF1 and RF2) is comparable to the dimensions of the initial dense layers of samples from the MW jet, while the total film thickness of MW samples is significantly higher (see Table 3).

The lateral nanostructuring of the smooth films was studied using AFM (see Fig. 5). An extremely low surface roughness of 0.3 nm (RMS) has been obtained. This property of the films permitted the application of ISR for a two-dimensional characterization of the local deposition. The ISR results, shown in Fig. 5, reproduce the maximum film thickness obtained with SEM of the film cross-sections (compare the image RF2-a in Fig. 5 with the right image in Fig. 4). The refractive index of the RF1 film, determined by ISR, was only slightly lower than for SiO_2, specifically 1.45 at wavelength $\lambda = 500$ nm. However, the refractive index of the RF2 film was considerably lower, about 1.38 at 500 nm. Since the carbon content was almost identical in both films, this indicates that RF2 has a lower density than RF1, which is in agreement with the results from IR spectroscopy below. Note, that the application of ISR on the samples deposited by means of the MW plasma jet is not possible due to extremely high surface roughness. The results from the morphological analysis of the coated samples are summarized along with the results of the chemical characterization in Table 3.

4.2. Chemical composition

The pronounced differences in the film structure requires a careful combination of analytic methods in order to characterize the chemical composition of films correctly considering the film thickness, surface roughness and physical limitations of the methods. We applied XPS analysis for the characterization of the elemental composition present on the surface of the deposited films. EDX analysis was carried out for the elemental composition in the bulk, particularly in the case of thicker samples (MW1 and MW2). The EDX analysis of thinner films (samples RF1 and RF2) is influenced by the substrate because of the higher signal generation depth (here: 200–500 nm). Therefore the analysis of the samples RF1 and RF2 was conducted using XPS and in situ sputtering of the films. Here, 50 nm of the film were removed by sputtering, before the chemical composition of the bulk was measured. Note that the information depth of XPS is limited to only several nm. Finally, the combination of EDX, XPS, and the sputtering technique provides the elemental composition on the surfaces and in the bulk separately. The infra-red spectroscopy of all samples has been applied as a complementary method to the previous technique in order to identify chemical functional groups, and to characterize the stoichiometry (SiO_x), porosity and trends concerning impurities (carbon content). Again, two approaches have been applied: transmission FTIR for smooth thin films (RF1 and RF2) and ATR-FTIR for thicker, absorbing samples (MW1 and MW2). The compilation of the main findings is shown in Table 3.

FTIR spectra of all films deposited from TTMS are compared in Fig. 6. The spectra show characteristic peaks of silica at about 800 and

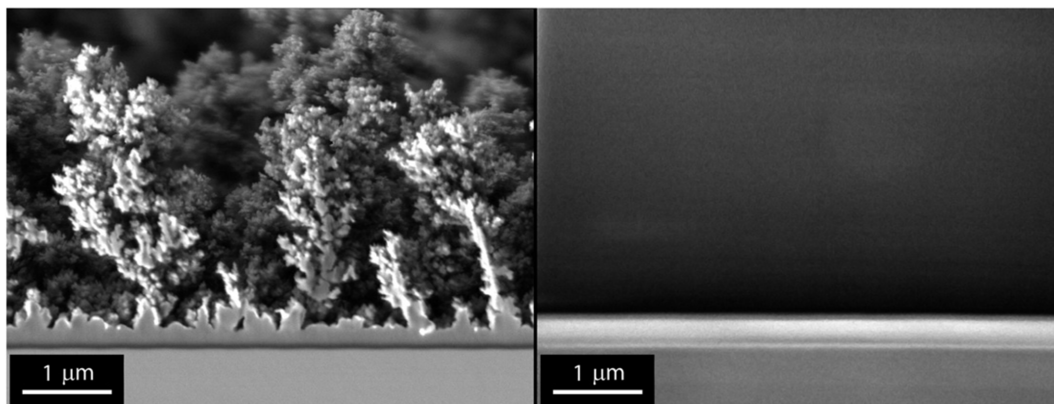

Fig. 4. Cross-sectional SEM micrographs of the films on silicon substrates: nanostructured MW2 film deposited in MW jet (left), compact smooth RF2 film deposited in RF jet (right).

Table 3
Summary of the film properties.

	RF1	RF2	MW1	MW2
Specific energy W/F [kJ cm^{-3}]	20	50	200	900
Structure[a]	SL	SL	SL + D	SL + D
Deposition rate [nm/s]	0.1[b]	0.4[b,a]	17[a]	10[a]
Maximum height [μm]	0.13[b]	0.35[b,a]	5[a]	3[a]
Roughness [nm]	0.3[c]	0.3[c]	–	SL: 100[d]
SiO_x stoichiometry [O]/[Si]	1.9[e] / 1.8[f]	2.1[e,f]	1.6[g] / 1.8[f]	2.1[g] / 2.2[f]
Residual carbon in bulk [%]	5[e]	4[e]	3[g]	1[g]
Total carbon on surface [%][h]	22	7	12	6

SL — single dense layer; D — structure of dendrites.
[a] SEM analysis.
[b] Imaging spectroscopic reflectometry.
[c] AFM analysis.
[d] SEM analysis using cross-section ion polishing.
[e] XPS analysis using the sputtering of the surface.
[f] FTIR analysis.
[g] EDX analysis.
[h] XPS analysis.

1070 cm^{-1} corresponding to the bending and antisymmetric stretching mode ('bulk mode', AS) of the Si–O–Si groups, respectively [27]. A transverse optical mode of Si–O–Si ('surface mode', TO) appears between 1130 and 1200 cm^{-1}. While the AS mode can be interpreted as diagnostics for the film stoichiometry, the characteristic of the TO peak can indicate the inner surface or porosity of films qualitatively. Indeed, the samples MW1 and MW2 exhibit a strong absorption of the TO peak (left flank of the AS mode) as expected from the SEM analysis of these samples. They are characteristic with their dendrite structure causing a large effective surface of the samples and thus an intensive excitation of the surface TO mode in the IR spectrum. The transmittance measurements, that could be performed down to 370 cm^{-1} for RF1 and RF2 films, confirm the existence of the peak at 450 cm^{-1} that is associated with the Si–O–Si rocking. Finally, absorption peaks at 1279 cm^{-1} and 920 cm^{-1} are related to the Si–CH_3 and silanol groups (Si–OH), respectively [28,29]. They indicate an (in)sufficiency of decomposition and oxidation of TTMS molecules by the plasma. Essential characteristic peaks are listed in Table 4.

Both series of experiments (RF and MW) exhibit the same trends regarding the absorption peak at 1279 cm^{-1}: with increasing specific energy a reduced Si–CH_3 signal at 1279 cm^{-1} can be observed. Please note that for MW1 the overall concentration of TTMS is two times higher (≈20 ppm) than for RF1, RF2, and MW2, therefore Si–CH_3 can appear in the spectra of MW1 easily, even if the specific energy at MW1 is higher than in the case of RF2. The deposition rate follows the same trend as the change of the Si–CH_3 peak: with the increase of the specific

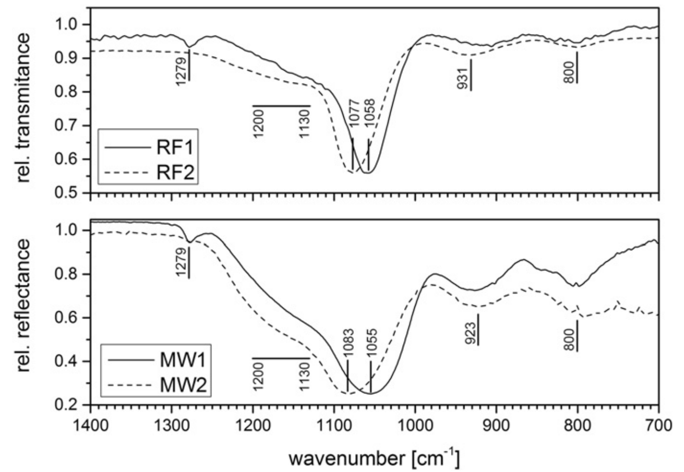

Fig. 6. Infrared spectra of the deposited films. Transmission FTIR (top), ATR-FTIR (bottom). The shift of the main absorption peak (1050–1080 cm^{-1}) to higher wavenumber indicates a higher stoichiometry of SiO_x and a broad absorption between 1200 and 1130 cm^{-1} reveals a large top or inner surface (roughness and/or porosity) of MW samples.

energy within the particular series (RFx and MWy) the deposition rate decreases. The positive correlation between the change of the deposition rate and the Si–CH_3 peak let us conclude that the increasing specific energy contributes to better oxidation – indeed, the Si–CH_3 peak disappears – improving the film density and retarding the growth. However, the presence of silanol termination groups suggests that the density of the deposited films (even the compact ones from RF process) is lower than SiO_2 glass. Further conclusion on the properties of the SiO_2 films can be drawn from the position of the AS mode in the spectrum. Its shift to lower wavenumbers can be related to several phenomena like carbon contamination [30], oxygen deficiency [31,32] and material densification [33]. Finally, these effects result in lower stoichiometry of the SiO_x. Moreover, the dependence of x on the position of the AS mode can be derived for the studied class of films precisely [19,34,35]. The obtained values are between 1.8 and 2.2. The samples RF1 and MW1 are stoichiometrically similar (1.8), while the ratio [O]/[Si] determined for samples RF2 and MW2 is higher, 2.1–2.2, than the stoichiometric ratio of pure SiO_2. This can be explained by the higher content of -OH terminating groups in RF2 and MW2. Indeed, the Si–OH absorption is higher for RF2 and MW2 films compared to RF1 and MW1, which on the other hand exhibit a higher concentration of carbon (Si–CH_3 peaks) and lower stoichiometry. Additionally, the –OH group is bond on a residual carbon, too. Water absorption peaks were not detected.

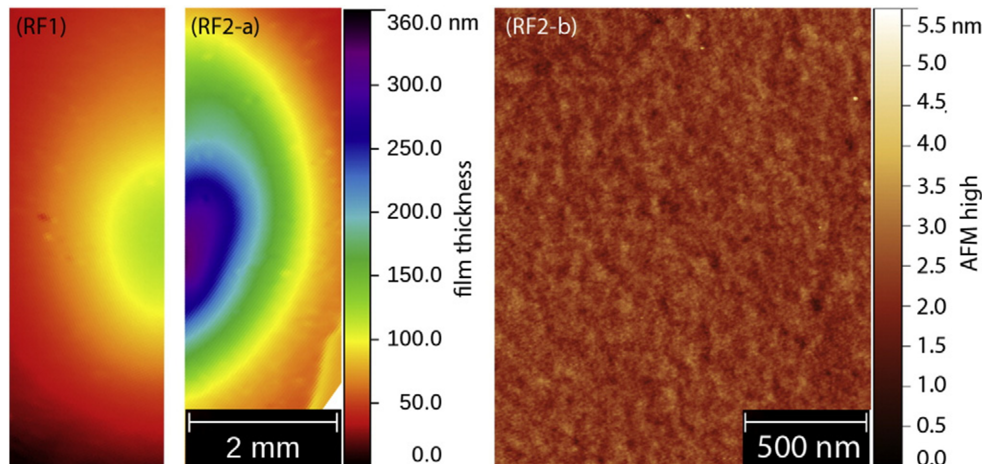

Fig. 5. Topography of the local deposition from TTMS using the RF jet. Film thickness of samples RF1 and RF2 is imaged using spectroscopic reflectometry (images RF1 and RF2-a), the surface roughness in the middle of the samples RF2 is visualized by AFM, RMS = 0.3 nm (image RF2-b).

Table 4
Characteristic infra-red absorption bands of SiO_x network.

Wavenumber [cm^{-1}]	Vibration mode	Appearance in samples			
		RF1	RF2	MW1	MW2
1279	$Si–CH_3$	w	n	w	n
1130–1200	Si–O–Si transv. optical (TO)	w	w	s	s
1050–1085	Si–O–Si asym. stretching (AS)	s	s	s	s
920–940	Si–OH stretching	w	m	m	m
800–810	Si–O–Si bending	w	w	m	m
450	Si–O–Si rocking	m	m	h	h

Notation: s — strong, m — medium, w — weak, n — no peak, and h — hypothetical. Indicators: $Si–CH_3$ — carbon content, TO — porosity or roughness, AS — stoichiometry, and Si–OH — oxidation grade.

The elemental analysis confirms a chemical similarity of all SiO_x samples. The oxygen atomic content of the films is between 60 and 67%, while the silicon atom percentage is 32–37%. The rest includes carbon (1–5%) and hydrogen atoms. However, hydrogen cannot be quantified by methods utilized here. The stoichiometric ratio $x = [O]/[Si]$ obtained from the elemental analysis (1.6–2.1) correlates very well with the prediction from FTIR analysis (1.8–2.2). Note, that the considerations on the correlation are based on the comparison of analytic methods specified by similar measurement depth (EDX vs. FTIR and sputtering XPS vs. FTIR). In contrast, the elemental composition of the film surfaces differs notably (see Table 3), e.g. the carbon atom percentage varies significantly between 6–22%. This deviation is mainly caused by two reasons: (1) The immanent difference between bulk and surface elemental composition. At the surface, a rearrangement of functional groups (particularly –OH) occurs, and a higher contamination by carbon and hydrocarbons (containing additional oxygen, too) is built up. (2) Evident differences in the film morphology as described in the previous subsection. For example, the carbon concentration of sample MW2 is six times higher at the surface than in the bulk, while the oxygen concentration on the surface changes only slightly (66–67%).

5. Discussion

5.1. On specific energy and temperature conditions

Primarily morphological properties and – despite the chemical similarity of studied films – small differences of the chemical composition are related to specifics of the plasma process, which shall be discussed here. Even with apparent different excitation scheme, we consider the differing power densities as the most significant disparity between the two set-ups. The geometry of the jets and precursor injection is similar in both experiments leading to comparable hydrodynamics and chemical kinetics. The power input in the MW jet was substantially higher than in the RF jet. Hence, qualitatively different PECVD processes could be expected. Indeed in a previous work [13], the atomic lines of Si (from dissociated TTMS) were observed in the optical emission spectra of the MW jet, while they could not be detected in the RF jet. Both set-ups, the MW jet and the RF jet differ considerably in numerous technical parameters: e.g. gas flow, average velocity, excitation frequency resulting in largely differing plasma physical characteristics (e.g. charge carrier kinetics, energies and concentrations, transport mechanisms and subsequently in different plasma-surface interactions). For instance, the observed growth rates differ essentially (up to 25–100 times higher in the MW jet). In an attempt to overcome the complexity of all these parameters we consider the energetic characterization and implement the concept of the Yasuda parameter for the comparison of the different deposition experiments and complement this concept by considering the different surface temperatures for the discussion of our results. The calculated Yasuda parameter (W/F) is shown in Tables 1 and 3. Note, that in the RF jet the variation of specific energy W/F (20–50 kJ cm^{-3}) is caused by the variation of the electric power, while in the MW jet (200–900 kJ cm^{-3}) it is due to the changing TTMS concentration.

It can be assumed, that the high specific energy input into the process initiates material synthesis already in the volume of the plasma, at least partially. Coalescence of nucleation centers in the plasma has potentially a coordination effect at the surfaces. They exhibit a high chemical affinity and low surface mobility. Considering the higher reaction temperatures and shorter reaction times at the higher electric power, the growth of nucleation centers can consequently explain the formation of dendrites at energies 200 and 900 kJ cm^{-3} in PECVD from TTMS (MW).

Above mentioned effects are definitely dependent on the temperature conditions at the plasma-surface interface during the deposition, too. However, a synchronous temperature diagnostics during the deposition has not been performed in this investigation. Nevertheless, the characteristics of both jets regarding the neutral gas temperature have been published in the previous studies [20,36,37]. The results suggest a maximum temperature of 420 K and 320 K during the deposition for the MW and RF jet, respectively. Thus, the ratio of temperature differences from the laboratory temperature is 3:1 (MW:RF) and hence smaller than the ratios of specific energies (in this study they are in the range from 4:1 to 45:1). In order to prove the specific effects of the surface temperature and its correlation with the Yasuda parameter, in situ thermography of the deposition would be desirable as well as the investigation of nanoparticle formation in the plasma. These are subjects to further studies.

5.2. On chemical properties and morphological structure

Regarding the carbon content, the increasing trends of energy per molecule from 20 to 50 kJ cm^{-3} (RF) and from 200 to 900 kJ cm^{-3} (MW) correlate with the decreasing trends of the bulk carbon concentration from 5 to 4% (RF) and from 3 to 1% (MW), respectively. The effect demonstrates the higher efficiency of precursor decomposition and increased oxidation of the SiO_x matrix at higher specific energy. Moreover, this energy dependent trend is related to an enhanced stoichiometric ratio from $x = 1.8$ to 2.1 for the RF deposition and 1.7 to 2.2 for the MW deposition. This observation is in accordance with the expectation based on the state of the art. Nevertheless, the difference in specific energies between the RF and MW experiments is about one order of magnitude. Therefore, a comparison between RF and MW series can be performed qualitatively at best, by discussing general trends. On the other hand it is a surprising result, that, given the largely diversified film structure produced by heavily differing specific energies between RF and MW experiments allows to distill similarities and parallels related to the chemical properties, which effectuate only small variations of the SiO_2 chemistry in the coatings produced by PECVD.

The dendritic nanostructures deposited with the high power MW jet could be used in applications, where a large specific surface is needed, e.g. heterogeneous chemistry, catalytic surfaces, sensors, hydrogen storage or battery separators. Further advantage of the films is their SiO_2 composition with low residual carbon content, which promises good chemical stability. The compact and smooth films produced with the low power RF jet could be used as a functional interlayer with low surface roughness for multilayer coatings. The presence of silanol groups in the films together with low carbon concentration makes the coating relevant for biochemical tests, too. The film properties could be even enhanced by selective functionalization. The results suggest that using a complex precursor molecule and tuning of input power can produce both nanostructures and smooth films (and their combinations) by a single process.

6. Conclusion

In this study we investigated atmospheric pressure PECVD based on tetrakis(trimethylsilyloxy)silane (TTMS). The usage of TTMS for thin film deposition by means of a radiofrequency non-thermal atmospheric pressure plasma jet (RF jet) is reported herewith for the first time. We

compared results from deposition experiments involving TTMS in two different plasma sources: an RF jet and a microwave plasma jet (MW jet). Surprisingly, it could be found, that – despite the dramatic specific energy differences between both jets – the chemical composition of the deposited films is very similar, close to SiO_2. However, largely differing film morphologies could be obtained covering the broad interval of deposition rates from 0.1 nm/s to 17 nm/s.

Nine different analytical approaches regarding film and surface analysis have been applied during this study in order to present a consistent picture of the morphological structure (SEM, cross-section polishing for SEM, AFM, imaging spectroscopic reflectometry) and chemical composition (transmission FTIR, ATR-FTIR, EDX, XPS, and sputtering XPS) of deposited films.

By deposition from TTMS with the MW jet intact dendritical nanostructures have formed. Their chemical composition resembles that of SiO_2, with only 1% contamination by residual carbon and can promote interesting applications that require chemically stable yet large effective surface areas. These properties qualify the coating for example for adsorption tests regarding surface sensor applications or as matrix surface for heterogeneous catalysis. On the other hand, the deposition by the RF jet demonstrates, that a comparable chemical composition of the film can be achieved with an energy input 18-times smaller than in the MW jet. Here, the resulting surface exhibits an extremely low surface roughness. The technological potential of the studied films demonstrates the relevance of investigations that are aimed to introduce precursor molecules of large and complex molecular structure into gas discharges at atmospheric pressure accenting the role of chemical functionalization and surface nanostructuring.

Acknowledgments

The authors thank David Nečas for help with ISR data analysis and Petr Klapetek for AFM measurements. The work has been funded in part by the following sources: 7th European Framework Program, project no. 316216, “PlasmaShape”; DFG, Transregio 24 “Fundamentals of Complex Plasmas”, project CZ.1.05/2.1.00/03.0086, funded by the European Regional Development Fund; project LO1411 (NPU I) funded by the Ministry of Education Youth and Sports of Czech Republic; “CEITEC — Central European Institute of Technology” (CZ.1.05/1.1.00/02.0068) from the European Regional Development Fund; and by project TE02000011 of the Czech Technology Agency.

References

[1] H. Nagel, A.G. Aberle, R. Hezel, Prog. Photovolt. Res. Appl. 7 (1999) 245–260.
[2] S.E. Alexandrov, N. McSporran, M.L. Hitchman, Chem. Vap. Depos. 11 (2005) 481–490.
[3] J. Schäfer, S. Horn, R. Foest, R. Brandenburg, P. Vašina, K.-D. Weltmann, Surf. Coat. Technol. 205 (2011) S330–S334.
[4] D. Gnanasekaran, K. Madhavan, B.S.R. Reddy, J. Sci. Ind. Res. 68 (2009) 437.
[5] B. Barwe, F. Riedel, O.E. Cibulka, I. Pelant, J. Benedikt, J. Phys. D Appl. Phys. 48 (2015) 314001.
[6] T. Maschmeyer, M.C. Klunduk, C.M. Martin, D.S. Shephard, J.M. Thomas, B.F.J. Johnson, Chem. Commun. (1997) 1847–1848.
[7] R. Duchateau, Chem. Rev. 102 (2002) 3525.
[8] G. Sievers, S. Mueller, A. Quade, F. Steffen, S. Jakubith, A. Krutha, V. Brueser, J. Power, Sources 268 (2014) 255–260.
[9] D.A. Loy, K.J. Shea, Chem. Rev. 95 (1995) 1431.
[10] I.L. Dubchak, V.E. Shklover, M.Y. Antipin, Y.T. Struchkov, V.M. Kopylov, A.M. Muzafarov, P.L. Prikhod'ko, A.A. Zhdanov, J. Struct. Chem. 23 (1982) 219.
[11] M. Bordeau, J. Dedier, E. Frainnet, J.-P. Fayet, P.J. Mauret, Organomet. Chem. 61 (1973) 91.
[12] A.I. Lazarev, The Vibrational Spectra and Structure of Silicates [in Russian], Nauka, Leningrad, 1968.
[13] J. Hnilica, J. Schäfer, R. Foest, L. Zajčková, V. Kudrle, J. Phys. D Appl. Phys. 46 (2013) 335202.
[14] H. Kim, H. Oh, C. Lee, D. Jung, J.H. Boo, Bull. Kor. Chem. Soc. 35 (2014) 2941.
[15] C. Tendero, C. Tixier, P. Tristant, J. Desmaison, P. Leprince, Spectrochim. Acta B 61 (2006) 2–30.
[16] L. Bárdos, H. Baránková, Thin Solid Films 518 (2010) 6705–6713.
[17] D. Trunec, Z. Navrátil, P. St'ahel, L. Zajíčková, V. Buršíková, J. Čech, J. Phys. D Appl. Phys. 37 (15) (2004) 2112–2120.
[18] D. Trunec, L. Zajíčková, V. Buršíková, F. Studnička, P. St'ahel, V. Prysiazhnyi, V. Peřina, J. Houdková, Z. Navrátil, D. Franta, J. Phys. D Appl. Phys. 43 (22) (2010) 225403.
[19] J. Schäfer, R. Foest, A. Quade, A. Ohl, K.-D. Weltmann, J. Phys. D Appl. Phys. 41 (2008) 194010.
[20] J. Schäfer, R. Foest, A. Quade, A. Ohl, J. Meichsner, K.-D. Weltmann, Eur. Phys. J. D 54 (2009) 211.
[21] J. Hnilica, V. Kudrle, P. Vašina, J. Schäfer, V. Aubrecht, J. Phys. D Appl. Phys. 45 (2012) 055201.
[22] M. Moisan, C. Beaudry, P. Leprince, Phys. Lett. 50 (1974) 125.
[23] J. Schäfer, R. Foest, A. Ohl, K.-D. Weltmann, Plasma Phys. Control. Fusion 51 (2009) 124045.
[24] D. Nečas, V. Čudek, J. Vodák, M. Ohlídal, P. Klapetek, J. Benedikt, K. Rügner, L. Zajíčková, Meas. Sci. Technol. 25 (2014) 115201.
[25] D. Franta, D. Nečas, L. Zajíčková, Opt. Express 15 (2007) 16230–16244.
[26] R. Foest, M. Schmidt, H. Gargouri, Eur. Phys. J. D 68 (2014) 23.
[27] C. Martinet, R.A.B. Devine, J. Appl. Phys. 77 (9) (1995) 4343–4348.
[28] D.R. Anderson, Infrared, Raman and Ultraviolet Spectroscopy, in: A.L. Smith (Ed.), Analysis of Silicones, Wiley-Interscience, New York 1974, p. 247 (Chapter 10).
[29] C. Rau, W. Kulisch, Thin Solid Films 249 (1994) 28–37.
[30] K. Aumaille, C. Vallée, A. Granier, A. Goullet, F. Gaboriau, G. Turban, Thin Solid Films 359 (2000) 188.
[31] L. He, T. Inokuma, Y. Kurata, S. Hasegawa, J. Non-Cryst. Solids 185 (1995) 249.
[32] A. Kučírková, K. Navrátil, L. Pajasová, V. Vorlíček, Appl. Phys. A Mater. Sci. Process. 63 (1996) 495.
[33] R.A.B. Devine, Trans. Mater. Res. Soc. Jpn. 8 (1992) 165.
[34] W. Kaiser, P.H. Keck, C.F. Lange, Phys. Rev. 101 (1956) 1264.
[35] P.G. Pai, S.S. Chao, Y. Takagi, G. Lucovsky, J. Vac. Sci. Technol. A 4 (1986) 690.
[36] J. Hnilica, V. Kudrle, L. Potočňáková, IEEE Trans. Plasma Sci. 40 (2012) 2925.
[37] J. Schäfer, Z. Bonaventura, R. Foest, Eur. Phys. J. Appl. Phys. 71 (2015) 20804.